Journal of
Synchrotron
Radiation

ISSN 0909-0495

Received 8 June 2004
Accepted 9 December 2004

# Linear and circularly polarized light to study anisotropy and resonant scattering in magnetic thin films

**Hélio C. N. Tolentino,[a]* Júlio C. Cezar,[a,b] Narcizo M. Souza-Neto[a,c] and Aline Y. Ramos[a,d]**

[a]LNLS, Laboratório Nacional de Luz Síncrotron, CP 6192, 13084-971, Campinas, SP, Brazil, [b]IFGW, Universidade Estadual de Campinas, CP 6165, 13083-970, Campinas, SP, Brazil, [c]Departamento de Física dos Materiais e Mecânica, IF-USP, São Paulo, SP, Brazil, and [d]LMCP, Laboratoire de Minéralogie-Cristallographie, UMR 7590, CNRS, Paris, France. E-mail: helio@lnls.br

The remarkable polarization properties of synchrotron light have lead to the advent of modern synchrotron-related spectroscopic studies with angular and/or magnetic selectivity. Here an overview is given of the prominent aspects of the polarization of the light delivered by a bending magnet, and some dichroic properties in X-ray absorption spectroscopy (XAS). Two studies developed at the Brazilian Synchrotron Light Laboratory are then reported, exemplifying the profit gained using linear and circular polarization of X-rays for the study of magnetic thin films and multilayers. Angle-resolved XAS was used in strained manganite thin films to certify a model of local distortion limited within the $MnO_6$ polyhedron. A pioneering experience of X-ray magnetic scattering at grazing incidence associated with dispersive XAS in a Co/Gd multilayer draws new perspectives for magnetic studies in thin films and multilayers under atmospheric conditions in the hard X-ray range.



**Keywords: X-ray absorption spectroscopy; X-ray dichroism and polarization; magnetic thin films.**

## 1. Introduction

The importance of synchrotron light in the investigation of new materials is well recognized nowadays. Synchrotron light sources deliver much more photons and with a larger brilliance compared with conventional tube sources. Furthermore, these sources owe their status to other intrinsic properties: a wide and continuous spectrum, which allows tuning the photon energy close to resonances, and well defined polarization states. Both aspects are of fundamental interest for the investigation of local atomic and electronic anisotropy, as well as local magnetic moment and magnetic order in magnetic systems.

In this paper we discuss the prominent aspects related to the use of linear and circularly polarized light emitted in a bending magnet, and present, as examples of this use in thin films and multilayers, two studies performed at the Brazilian Synchrotron Light Laboratory (LNLS). We begin (§2) with an introduction to synchrotron light emission and polarization properties, followed by the description of the optical set-ups and how they affect the polarization states. We limit this approach to the light produced by bending magnets, since the studies presented were performed on such devices. We introduce (§3) X-ray absorption spectroscopy (XAS) and some dichroic properties of the spectra related to the polarization of the photons. Examples are presented in the two next sections. The linear polarization of the photons (§4) has been exploited at the double-crystal monochromator XAS beamline to study the local distortion in strained manganite thin films. The dispersive XAS beamline, well suited for the X-ray magnetic circular dichroism (XMCD) technique owing to its intrinsic stability, has been associated with the grazing-incidence technique for measuring (§5) resonant scattering in a Co/Gd magnetic multilayer. These two examples highlight the potential of using the polarization properties of synchrotron light in XAS studies of the atomic, electronic and magnetic properties of materials.

## 2. Synchrotron light sources and polarization properties

The aim of this section is to recall some essential features of the light emitted by relativistic electrons within the poles of a bending magnet in a storage ring. This section is based on the development made by J. D. Jackson (Jackson, 1975). The properties of the electromagnetic radiation emitted by these electrons are related to their trajectory and motion. The electrons revolve along a closed trajectory with quasi-circularly bent parts, which makes the acceleration well defined and

radial. Let us consider the special situation of a point charge in instantaneously circular motion, so that its acceleration is perpendicular to its velocity (Fig. 1). In a synchrotron, one deals with the ultra-relativistic case where $\gamma \gg 1$, with $\gamma$ defined as the energy of the electrons divided by its rest energy $mc^2$. At LNLS, operating with an electron energy of 1.37 GeV, $\gamma = 2680$; for a high-energy machine, like APS in Chicago operating at 7 GeV, $\gamma = 13700$.

The propagating radiation field generated by a point accelerated charge can be written as a function of its normalized velocity ($\vec{\beta} = \vec{v}/c$) and acceleration ($\vec{\beta}' = \mathrm{d}\vec{\beta}/\mathrm{d}t$),

$$\vec{B}(\vec{r}, t) = [\hat{n} \times \vec{E}]_{\mathrm{ret}}, \tag{1}$$

$$\vec{E}(\vec{r}, t) = \frac{e}{c}\left[\frac{\hat{n} \times \{(\hat{n} - \vec{\beta}) \times \vec{\beta}'\}}{(1 - \vec{\beta} \cdot \hat{n})^3 R}\right]_{\mathrm{ret}}, \tag{2}$$

where both $\vec{E}$ and $\vec{B}$, evaluated at the retarded time, are transverse to the radius vector $\hat{n}$ and decay as $1/R$, the distance from the source to the observer. The Poynting's vector $[\vec{S} \cdot \hat{n}]_{\mathrm{ret}} = (c/4\pi)|\vec{E}|^2$ gives the density of propagating energy.

The specific spatial relationship between $\vec{\beta}$ and $\vec{\beta}'$ determines the detailed angular distribution. However, the relativistic effect, represented by the presence of the factors $(1 - \vec{\beta} \cdot \hat{n})$ in the denominator, dominates the whole angular distribution and gives rise to the collimation of the emission. By integrating the energy per unit area per unit time during a finite period of acceleration, one can deduce the power radiated per unit solid angle,

$$\frac{\mathrm{d}P(t')}{\mathrm{d}\Omega} \simeq \frac{2e^2}{\pi c^2}\frac{\gamma^6\beta^2}{(1 + \gamma^2\Psi^2)^3}\left[1 - \frac{4\gamma^2\Psi^2\cos^2\varphi}{(1 + \gamma^2\Psi^2)^2}\right]. \tag{3}$$

In the ultra relativistic approximation ($\gamma \gg 1$), the root mean square angle of emission $\langle\Psi^2\rangle^{1/2}$ is given by $\gamma^{-1}$. The emission is essentially within a cone with a very small opening about the orbit plane. In the opposite situation, for an accelerated charge in non-relativistic motion, the angular distribution of the emitted radiation shows a simple $\sin^2\varphi$ behavior, where $\varphi$ is measured with respect to the direction of acceleration.

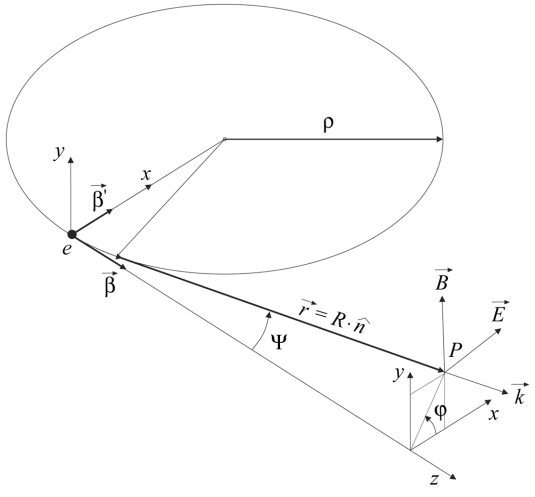


**Figure 1**
Geometry and notation used to calculate the synchrotron radiation emission.

The total power radiated can be found by integrating the above equation over all angles,

$$P(t') = \frac{2}{3}\frac{e^2\beta'^2}{c^2}\gamma^4. \tag{4}$$

This power has a broad band in the frequency space that comes as a counterpart of the collimation. An observer, who sits in the laboratory, far from the moving point charge, sees the emission only when the charge travels along a very specific portion of the circular trajectory, limited to about $1/\gamma$, and receives light as short pulses. The Fourier transform of the delta-like function in time space is spread over a wide range in the frequency space, so that the synchrotron emission has a continuous 'white light' distribution (Raoux, 1993).

The vectorial double cross product in the transverse electric field generated by the relativistic moving charge gives a vector with two components, one along $\hat{n} - \vec{\beta}$ and the other along the acceleration $\vec{\beta}'$,

$$\hat{n} \times \{(\hat{n} - \vec{\beta}) \times \vec{\beta}'\} = (\hat{n} - \vec{\beta})(\hat{n} \cdot \vec{\beta}') - \vec{\beta}'(1 - \hat{n} \cdot \vec{\beta}). \tag{5}$$

$\hat{n} - \vec{\beta}$ is roughly the difference between two almost collinear unit vectors, therefore it is orthogonal to $\hat{n}$. If one considers the emission right above the plane of the circular orbit ($\varphi = \pi/2$), $\hat{n} - \vec{\beta}$ will be a vector perpendicular to the orbit plane and $\vec{\beta}'$ a vector in this plane. Since the acceleration is the derivative of the velocity, one of the components of the electric field is phase shifted by $\pi/2$ with respect to the other. This is at the origin of the circular polarized light.

The energy radiated per unit frequency interval per unit solid angle is given by

$$\frac{\mathrm{d}^2 I}{\mathrm{d}\omega\,\mathrm{d}\Omega} = \frac{3e^2}{4\pi^2 c}\left(\frac{\omega}{\omega_{\mathrm{c}}}\right)^2\gamma^6\left(\frac{1}{\gamma^2} + \Psi^2\right)^2 \times \left[K_{2/3}^2(\xi) + \frac{\Psi^2}{(1/\gamma^2) + \Psi^2}K_{1/3}^2(\xi)\right], \tag{6}$$

where $K_{1/3}(\xi)$ and $K_{2/3}(\xi)$ are second-rank Bessel functions, with $\xi = (\omega\rho/3c)[(1/\gamma^2) + \Psi^2]^{3/2}$. Parameter $\omega_{\mathrm{c}} = (3c/2\rho)\gamma^3$ defines the critical energy, $E_{\mathrm{c}} = \hbar\omega_{\mathrm{c}}$, that separates the total emission in two equal parts. At LNLS, $E_{\mathrm{c}}$ is 2.08 keV, characterizing a low-energy storage ring (Rodrigues *et al.*, 1998). The first term in the square brackets corresponds to radiation polarized parallel to the orbit and the second to radiation polarized perpendicular to that plane. For $\Psi = 0$ the photons are strictly linearly polarized in the plane. Fig. 2 shows the calculated intensity of the components parallel ($\sigma$) and perpendicular ($\pi$) as a function of the displacement angle ($\Psi$), at the critical energy $E_{\mathrm{c}}$ and at $4E_{\mathrm{c}}$, energy close to the working range of the XAS experiments. One can remark that in the high-energy region the cone of emission becomes narrower.

The degree of linear polarization in the horizontal plane $P_{\mathrm{L}}$ and of circular polarization $P_{\mathrm{C}}$ are given by

$$P_{\rm L} = \frac{A^2 - B^2}{A^2 + B^2}, \qquad P_{\rm C} = \frac{2AB}{A^2 + B^2},$$

where

$$A = \left(\frac{1}{\gamma^2} + \Psi^2\right) K_{2/3}(\xi), \quad B = \left(\frac{1}{\gamma^2} + \Psi^2\right)^{1/2} \Psi K_{1/3}(\xi). \quad (7)$$

Circularly polarized light can then be obtained by selecting the incident beam slightly above or below the orbital plane.

We limited this section to the polarization properties of the light produced in a bending magnet, since our purpose is to give the basic principles of the emission and also because this was the source used in the studies developed at the LNLS. Circularly polarized light is actually more commonly obtained by using special insertion devices like wigglers or undulators (Raoux, 1993; Als-Nielsen & McMorrow, 2001). To a lesser extent, optical devices like quarter-wave plates are used to transform the linearly polarized light in the orbital plane into circularly polarized light (Giles *et al.*, 1994).

In a real synchrotron, the average over the finite slit aperture and the electron emittance, which is roughly the product of the electron beam size and its divergence, attenuate the degree of polarization by a few percent. The effects of the optical elements are much larger and only these effects are considered in the scope of this paper. Mirrors at grazing incidence reflect both components of the beam in the same way and the effect on polarization ratio can always be neglected. A conventional XAS monochromator involves two reflections from silicon or germanium crystals with the horizontal ($\sigma$) component of the beam lying perpendicular to the diffraction plane (Fig. 3*a*). For this component, the polarization factor in the reflected beam is equal to 1 and, neglecting absorption, the beam is totally reflected within the Darwin width (James, 1965). The vertical ($\pi$) component of the beam lies in the diffraction plane and is reduced according to the factor $|\cos 2\theta|^2$, where $\theta$ is the Bragg angle of diffraction. The total emitted power is almost unchanged (Fig. 4*a*) and the linear polarization is enhanced (Fig. 4*b*). In the case of the

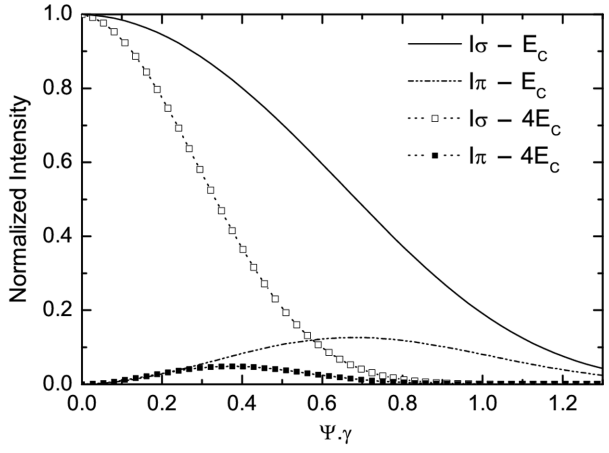


**Figure 2**
Normalized intensity calculated for the emitted radiation with the polarization vector parallel ($\sigma$) and perpendicular ($\pi$) to the electron orbit plane, as a function of the displacement angle from this plane ($\Psi\gamma$), at the energies $E_{\rm c}$ = 2080 eV (lines) and $4E_{\rm c}$ = 8320 eV (symbols). For the LNLS storage ring, $\gamma^{-1}$ = 0.373 mrad.

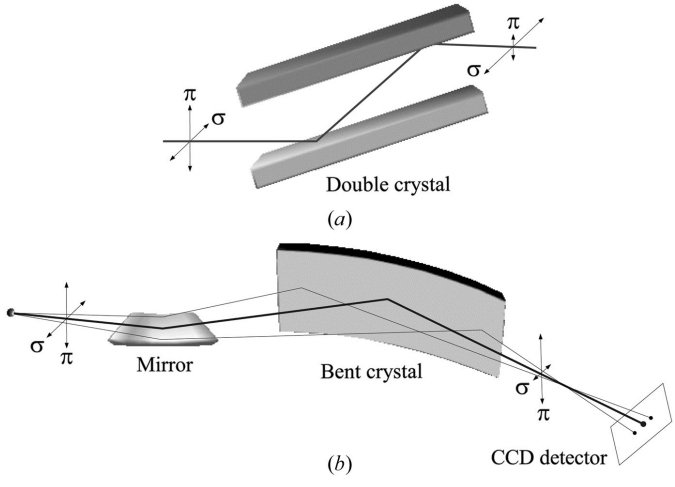


**Figure 3**
Schematic view of the optics for (*a*) the conventional double reflection monochromator, and (*b*) the dispersive monochromator, where an energy bandpass is selected by a bent crystal.

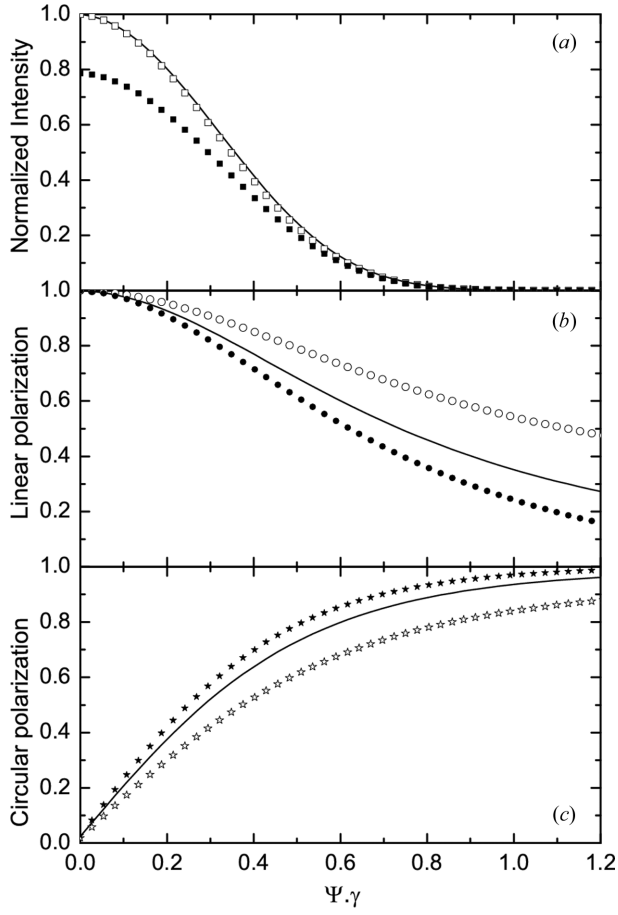


**Figure 4**
Normalized intensity (*a*), linear polarization (*b*) and circular polarization (*c*) ratios at the Gd $L_3$ edge ($E$ = 7243 eV), calculated for the photon beam produced by the source (solid line) and after diffraction by the dispersive (closed symbols) and the double-crystal monochromator (open symbols), as a function of the displacement angle ($\Psi$) from the electron orbit plane.

dispersive XAS monochromator (Dartyge, Depautex *et al.*, 1986) (Fig. 3*b*), there is only one Bragg diffraction. The horizontal ($\sigma$) component lying in the diffraction plane is affected by the factor $|\cos 2\theta|$. The vertical ($\pi$) component is not affected. The total emitted power is reduced (Fig. 4*a*), but circular polarization is significantly enhanced (Fig. 4*c*).

## 3. Polarized light and X-ray absorption spectroscopy

### 3.1. X-ray absorption spectroscopy

An X-ray absorption spectrum corresponds to the variation of the absorbing coefficient with the energy of the photons (Koningsberger & Prins, 1988). The absorption edge is the drastic variation of this absorption coefficient for a photon energy close to the energy of a core-level electron. It corresponds to the transition from a deep core electron level of a selected atom to empty levels above the Fermi energy. The ratio between the absorbed energy and the incident photon flux, called the absorption cross section, $\sigma(\omega)$, is given by the summation over all possible final states of the transition probability from the initial state $i$ to a final state $f$. Each probability is expressed by Fermi's golden rule as the square matrix related to the Hamiltonian describing the interaction of X-rays with the electrons of the matter. This interaction Hamiltonian can be approximated in the perturbation theory and expressed as a multipolar expansion. The first term of the expansion is the dipole electric term, followed by the dipole magnetic and the quadrupole electric terms, several orders of magnitude smaller (Fontaine, 1993). In the so-called electric dipole approximation, these last terms are neglected and the electromagnetic field is taken as constant in the initial state site. The absorption cross section then reads

$$\sigma(\omega) = 4\pi^2\alpha\hbar\omega \sum_{if} \left|\langle f|\hat{\varepsilon}\cdot\vec{r}|i\rangle\right|^2 \delta(E_f - E_i - \hbar\omega)\rho(E_f), \quad (8)$$

where $\alpha \equiv e^2/(\hbar c)$ is the fine structure constant. The delta Dirac distribution ensures the energy conservation and $\rho(E_f)$ is the empty density of states.

The chemical selectivity is the main appeal of X-ray absorption spectroscopy. Each element of the material can be selected by tuning the X-ray photon energy in the region of one of its core levels and experimental data can be collected element by element.

The final and initial states in the matrix cross section can be expressed as a combination of spherical harmonics and their composition obey the Wigner–Eckard theorem. The resulting selection rules are the second major characteristic of X-ray absorption spectroscopy. In the dipole approximation these selection rules state $\Delta s = 0$, $\Delta l = \pm 1$, $\Delta j = \pm 1, 0$. At the $K$ and $L_1$ ($l = 0$) edges, 1*s* or 2*s* electrons are excited to final empty levels with $p$ symmetry ($l = 1$) and the transition to $d$ levels is forbidden ($\Delta l = 2$). At the $L_{2,3}$ edges a 2*p* electron ($l = 1$, $j = 3/2, 1/2$) is excited to vacant $d$ levels ($\Delta l = 1$) and, with a much weaker transition probability, to empty $s$ levels ($\Delta l = -1$). X-ray absorption is then a selective probe for the angular momentum of empty levels.

The selection rules relative to the principal, orbital and total quantum number do not depend on the polarization of the interacting photon. However, the Wigner–Eckard theorem forces a last selection rule to the magnetic orbital quantum number $m$, and this rule depends on the polarization of the photons. If we consider non-magnetic systems and linear polarization only, the dipole operator does not affect the magnetic orbital quantum number and the selection rule is $\Delta m = 0$. If circularly polarized photons are used, this rule should be modified to take into account the helicity of the photons. The modifications of this selection rule are at the base of the interpretation of the X-ray magnetic dichroism that will be discussed in §3.3.

In summary, X-ray absorption spectra contain information about the ground state of the selected element in a material: local symmetry, oxidation and spin states, spin–orbit coupling in the 2*p* and 3*d* orbitals, crystal field, covalence and charge transfer. As a matter of fact, in the case of 3*d* transition metals, essential structural information is obtained from the $K$ edges, while more magnetic and electronic information is usually deduced from the $L_{2,3}$ edge.

Interpretation of X-ray absorption data can be carried out using basically two approaches. The monoelectronic approach is used in band structure or multiple-scattering calculations. Except the electron which has absorbed the photon, all electrons of the system are supposed to remain passive in the absorption process, and the correlations among electrons are neglected (Natoli *et al.*, 1980) or taken as an overall reduction term (Rehr & Albers, 2000). These approximations oversimplify the description of the X-ray absorption spectra in the case of localized final states. This is the case of the $L_{2,3}$ edge of transition-metal elements, that requires a multi-electronic approach (DeGroot, 1994). Nevertheless, monoelectronic models give a good description of the delocalized final states for systems where the electrons are weakly correlated. They are adequate for many studies in the hard X-ray range ($0.5 < \lambda < 5$ Å) and especially for the examples presented in this paper.

### 3.2. Linear dichroism in X-ray absorption spectroscopy

The polarization dependence of the intensity of the X-ray absorption spectra can be derived quite generally from the angular dependence of the transition matrix elements involved in the expression of the X-ray cross section. A thorough account of the angular dependence of the X-ray absorption spectra, including dipole and quadrupole effects, was given by Brouder several years ago (Brouder, 1990). Detailed formulae to analyze the experimental spectra can be found in this reference and we reduce the scope of this paragraph to the expression of the simple concepts.

Let us assume that the X-rays are linearly polarized light, $\hat{\varepsilon} = \hat{x}$, and recall that in the dipole electric approximation the square matrix element can be written $|\langle f|\hat{\varepsilon}\cdot\vec{r}|i\rangle|^2$. The case of $K$ (or $L_1$) shell excitation is easy to visualize. The initial $s$ state is isotropic. The vector matrix elements point in the same direction as the $p$-component of the final-state orbital on the

excited atom and thus the polarization dependence of the total matrix element can be expressed as a function of the angle $\theta$ between the direction of the electric field vector and the direction of the largest amplitude of the final-state orbital, that is the direction of the bond length. We should note that the $K$-shell excitations exhibit the strongest polarization-dependent effects because of the directionality of the $p$ component in the final state, and has been consequently the earliest stated and the more widely studied (Stern, 1974). The case of $L_2$ and $L_3$ excitations need a little more mathematical treatment but elegant derivations have also been documented (Heald & Stern, 1977; Haskel, 1998).

In anisotropic media the polarization dependence of the absorption cross section has the same structure as the dielectric constant. It is properly described by a tensor of rank 2, whose expression depends on the point group of the media. For samples with cubic point symmetry the absorption cross section is isotropic. The simplest expression of the dichroic effect is obtained for non-cubic samples, with a rotation axis of order greater than 2, where one can find two different cross sections. For this particular case, and expressing in terms of the linear absorption coefficient $\mu \propto \sigma$, one defines two parameters: $\mu_{\parallel}$ stands for the absorption coefficient when the electric vector lies in a plane orthogonal to the rotation axis, and $\mu_{\perp}$ is the coefficient when the electric vector is along the rotation axis. For any given orientation of the electric vector, measured by the angle $\theta$ related to that rotation axis, $\mu(\theta)$ reads

$$\mu(\theta) = \mu_{\parallel} \sin^2\theta + \mu_{\perp} \cos^2\theta. \quad (9)$$

We should note that this expression, largely known and used, is valid over the whole XAS energy range. As it is only related to the full point group symmetry of the material, it does not depend on the type ($K$, $L$, $M$) of X-ray excitation. One can readily realise that selective pieces of information can be extracted using angle-resolved XAS, as long as oriented samples are available. This tool, originating from the dot product $(\hat{\varepsilon} \cdot \vec{r})$ in the cross section, enhances the sensitivity of XAS to probe very tiny differences in anisotropic systems, like surfaces (Magnan *et al.*, 1991), anisotropic single crystals (Tolentino *et al.*, 1992; Gaudry *et al.*, 2003), multilayers (Pizzini *et al.*, 1992) or oriented films (Souza-Neto *et al.*, 2003).

### 3.3. X-ray magnetic dichroism

X-ray magnetic circular dichroism (XMCD) in X-ray absorption has been shown to be a unique element-selective magnetic probe (Ebert, 1996). The origin of XMCD is a local anisotropy of the absorbing atom resulting from the expected value of the local magnetic moment $\langle \vec{m} \rangle$. The magnetic field breaks the local symmetry of the absorber and lifts the degeneracy of the Zeeman energy levels. Then the photoelectron transition depends on the helicity of the photon polarization. The XMCD signal is the difference between the absorption cross sections with circularly left and right polarization.

If the X-ray absorption experiment is performed using circularly polarized photons, the selection rule for the magnetic orbital quantum number takes into account the helicity of the photons: $\Delta m = \pm 1$. $\Delta m = +1$ for left-handed polarization and $\Delta m = -1$ for right-handed polarization. In a magnetic compound the XMCD signal originates from the difference in the population of the levels with $m$ and $-m$ magnetic numbers. We recall that the interaction Hamiltonian does not act on the spin and XMCD results from the interaction between spin and orbital momentum, which couples the spin and the real space. In a simplified view, the XMCD signal is expressed as $R_{\mathrm{XMCD}} = P_{\mathrm{C}} P_e \Delta\rho/\rho$, where $\Delta\rho/\rho$ is the normalized spin polarized density of states (Schütz *et al.*, 1987). $P_{\mathrm{C}}$ is the circular polarization ratio and $P_e$ is a Fano-like factor giving the probability for the excited electron to be spin polarized. In the atomic limit, typical values of $P_e$ are 0.01 for $K$ excitations, $-0.5$ for $L_2$ and 0.25 for $L_3$ excitations. This simple model has proved to be useful for the interpretation of a large number of systems with rather delocalized final states (Baudelet *et al.*, 1991; Giorgetti *et al.*, 1993).

When the Hamiltonian is reduced to the electric dipole term, reversing the magnetic field or the circular polarization yield to the same result and most of the experiments are performed with a constant helicity with a magnetic field parallel or anti-parallel to the X-ray beam.

Like XMCD, X-ray resonant magnetic scattering (XRMS) probes the spin-polarized density of empty states above the Fermi level. In a quantum mechanical picture, the photon excites to a higher unoccupied level a core electron that decays back to the initial state emitting a photon of the same energy. The description of this process therefore involves emission *via* an intermediate state and requires second-order perturbation theory. Sensitivity to magnetism arises from the Pauli exclusion principle and the exchange-induced splitting of the Fermi level and is reinforced by the strong enhancement of magnetic effects when the photon energy is close to an absorption edge (Gibbs *et al.*, 1988; Hannon *et al.*, 1988). The XRMS signal is measured by the intensity asymmetry ratio $R_{\mathrm{XRMS}} = (I^+ - I^-)/(I^+ + I^-)$, where $I^+$ and $I^-$ are the intensities scattered for the opposite directions of an applied magnetic field.

## 4. Local anisotropy in perovskite thin films

The remarkable properties of hole-doped manganites show drastic sensitivity to small changes in their structural parameters and the form of the samples (Fontcuberta *et al.*, 1996; Millis, 1998; Salamon & Jaime, 2001). The magnetism and transport properties of manganites films differ significantly from those of the bulk material and are dependent on the film thickness (Millis *et al.*, 1998; Prellier *et al.*, 2001). Such a characteristic has been associated with the strain induced by the lattice mismatch. The understanding of the effects of the strains on the local structural parameters is crucial to explain the behavior of manganite thin films and multilayers.

We used angle-resolved XAS to characterize the local atomic structure around the manganese ions in

$La_{0.7}Sr_{0.3}MnO_3$ (LSMO) thin films epitaxically grown by pulsed laser deposition over $SrTiO_3$ (STO) and compressive $LaAlO_3$ (LAO) substrates. The small lattice mismatch between LSMO, STO and LAO allows a pseudomorphic growth and almost fully constrained conditions for film thicknesses below 100 nm and 40 nm, respectively (Ranno *et al.*, 2002): 1% in-plane tensile strain for STO and 2% in-plane compressive strain for LAO substrate.

We were looking for a dichroic signal around manganese to characterize a possible local anisotropy induced by the substrate. We took full benefit of the linear polarization of the synchrotron light to perform angle-resolved measurements and probe selectively atomic bond lengths in the plane and out of the plane of the films. According to Natoli's rule (Natoli, 1984), the energy position of the $1s \rightarrow 4p$ excitation scales as the bond length squared ($E - E_0 \propto R^2$), where $E_0$ is an energy close to the onset of the edge. It is possible to follow bond length changes by carefully looking at the energy position, that is accurately obtained thanks to the sharp rising edge.

Angle-resolved X-ray absorption experiments were performed at the D04B-XAS beamline of the LNLS (Tolentino *et al.*, 2001) at the Mn *K* edge (6539 eV). The monochromator was a Si(111) channel-cut. An ion chamber monitored the incident beam and data were collected in the fluorescence mode using a Ge 15-element solid-state detector. 0.5 mm slits selected the beam in the orbit plane ($\Psi = 0$) with an acceptance of 0.03 mrad. The light on the sample was predicted to be more than 99% linearly polarized. The films were set on a goniometer with the rotation axis perpendicular to the orbit plane. The experimental spectra were taken in two geometries: with the electric field of the incident linearly polarized photon beam set approximately parallel ($\mu_\parallel$) and perpendicular ($\mu_\perp$) to the film surface. XAS spectra were collected in the near-edge range of 6440 to 6700 eV with energy steps of 0.3 eV. The energy calibration of the edge was carefully monitored by simultaneous comparison with a Mn metal foil reference and the spectra were normalized at about 150 eV above the edge. This allows the edge structure in all experimental spectra to be compared in position and intensity, and energy shifts as small as 0.1 eV are certified.

The experimental XAS spectra of the tensile (STO substrate) and the compressive (LAO substrate) strained films are shown in Fig. 5(*a*). Taking the out-of-plane ($\mu_\perp$) spectra as reference, we observe energy shifts of the main $1s \rightarrow 4p$ transition among spectra collected in the two orientations: the shift is −0.4 eV for the tensile film and +0.9 eV for the compressive film. This result shows that in the LSMO/STO film the average Mn—O bond length in the film surface direction is greater than the same bond distance in the perpendicular direction to the film surface. In the opposite case, in the LSMO/LAO film, this in-plane average bond length is smaller than the out-of-plane bond distance, with a scale factor of approximately 2 in the energy shift.

From the X-ray diffraction results on these samples (Ranno *et al.*, 2002), and following Natoli's rule, energy shifts in opposite directions for tensile and compressive films were expected. We should note, moreover, that the ratio of the amplitude of the energy shifts (1:2) is approximately the same as the ratio of the long-range strain factor (∼1% for tensile and ∼2% for compressive) among these films. This direct proportionality between the modifications on the cell parameters and the local octahedral modifications indicates that the strain should be fully accommodated by changes in the coordination polyhedra ($MnO_6$), without any modification of the Mn—O—Mn angle (Souza-Neto *et al.*, 2004*a*).

*Ab initio* self-consistent field calculations in the full multiple-scattering formalism (Ankudinov *et al.*, 2002) were performed to address more precisely the actual consequence of the distortion of the octahedron on the near-edge XAS spectra and especially to investigate how far local distortion may account for the difference observed experimentally. The definition of the electric field vector polarization in relation to the atomic structure orientation, and then all the photoelectron scattering terms, are weighted using equation (9) presented in §3. This procedure enables us to calculate independently the information from the different angular contributions to the absorption. Simulations were performed in a LSMO cluster considering isotropic $MnO_6$ and anisotropic octahedral distortions. As expected for the isotropic case, the spectra do not show any modification in position and shape of

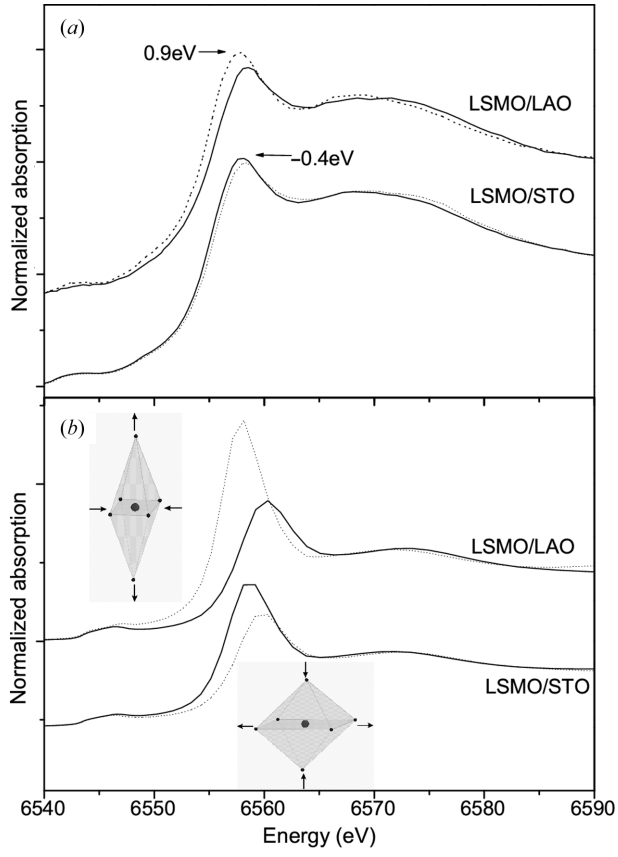


**Figure 5**
(*a*) Experimental XAS spectra at the Mn *K* edge for the tensile ($SrTiO_3$) and compressive ($LaAlO_3$) LSMO films in the plane (solid line) and perpendicular to the film plane (dotted line). The energy shifts are in opposite directions and scaled in amplitude by a factor of 2. (*b*) *Ab initio* XAS calculations considering tetragonal distortion of the $MnO_6$ octahedron and for the in-plane and out-of-plane contributions.

the edge main line among in-plane and out-of-plane situations. The calculations shown in Fig. 5(*b*) were performed for 21-atom clusters with tetragonal distortion using local order parameters scaling with the crystallographic cell parameters of the films (Souza-Neto *et al.*, 2004*b*). The calculated structures reproduce well the main features of the experimental results. They account as well for the energy shift, in amplitude and direction, as for the relative reduction in amplitude of the main peak close to the edge, among the two orientations and for each film (Souza-Neto *et al.*, 2004*c*). Based on these calculations, we validate the model of tetragonal distortion of the $MnO_6$ octahedron, suggested by experimental XANES spectra. This model is in agreement with extended X-ray absorption fine-structure results (Ramos *et al.*, 2003; Souza-Neto *et al.*, 2004*a*) and leads to the conclusion that the tilt angle Mn—O—Mn among adjacent octahedra is not, or little, changed (Souza-Neto *et al.*, 2004*a*). Actually the model of tetragonal distortion is not the unique model that may account for the experimental data. Orthorhombic or slightly monoclinic distortions cannot be totally ruled out only from XANES data (Souza-Neto *et al.*, 2003). However, the most important result remains unchanged: the coordination octahedron accommodated most of the distortion induced by the strain. We conclude that this distortion, tending to localize the charge carriers, is the driving parameter in the modifications of the magnetic and transport properties observed in thin films with respect to bulk systems (Souza-Neto *et al.*, 2003, 2004*a*).

## 5. Resonant scattering from films and multilayers

During the last decade, with the dramatic increase in the technological interest devoted to magnetic thin films and multilayers, resonant scattering in the soft X-ray range has progressively risen as a powerful tool especially adapted to the study of this class of material (Kao *et al.*, 1990; Tonnerre *et al.*, 1995; Sacchi *et al.*, 1998). However, it is worth noting that, during the same period, very few experiments were attempted in the hard X-ray domain (Dartyge, Fontaine *et al.*, 1986) in spite of the great advantage arising from the possibility of working under a variety of extreme conditions. Examples of the application of hard-X-ray XRMS can be found only recently in the literature with the works of Seve *et al.* and Jaouen *et al.* on the 5*d* electronic states across the rare-earth layers in Ce/Fe and La/Fe multilayers (Seve *et al.*, 1999; Jaouen *et al.*, 2002).

A prototype experiment to study resonant scattering over a wide energy range has been recently set up at the dispersive XAS beamline of LNLS (D06A-DXAS) (Tolentino, Cezar, Watanabe *et al.*, 2004). This beamline is equipped with an 800 mm-long Rh-coated mirror, working at a grazing angle of 4 mrad. The mirror bending mechanism allows vertical beam collimation or focusing to less than 500 µm at the sample position. A curved Si(111) crystal monochromator selects radiation from a bending-magnet source in the X-ray range from 5 keV up to 14 keV and focuses it to a 200 µm image. The detection is handled with a modified CCD camera. The energy–direction correlation coming out from the monochromator is transformed into an energy–position correlation along the lateral dimension of the CCD detector. Further descriptions of the beamline are published elsewhere, together with the commissioning results (Tolentino, Cezar, Souza-Neto *et al.*, 2004; Tolentino, Cezar, Watanabe *et al.*, 2004).

Experiments have been performed at grazing incidence to the surface of the films, close to the external total reflection condition (Als-Nielsen & McMorrow, 2001). In this reflectivity mode, the vertical dimension of the CCD detector is used to collect the X-rays scattered at different angles. The sample holder is fit with a goniometer with a horizontal axis, allowing alignment of the sample at grazing incidence angles with a resolution of 0.005°. A 100 µm slit in front of the sample holder limited the vertical beam. An electromagnet was used to apply a field of up to 500 G in the plane of the sample and along the propagation direction of the beam. The asymmetry ratio $R_{XRMS}$ is obtained by flipping the applied field.

The preliminary experiment was performed on a multilayer structure formed by the alternate deposition of 1 nm of Co and 0.2 nm of Gd, repeated 40 times. Both the Co *K* and the Gd $L_3$ edges are accessible and close to each other (7709 eV and 7243 eV), keeping very similar experimental conditions. Co is present in large amounts (about 40 nm) and carries a high magnetic moment while the amount of Gd is reduced (about 30 atomic layers) and carries a low magnetic moment at room temperature. On the other hand, the dichroism effect on the Co *K* edge is much smaller than for the Gd $L_3$ edge, so that similar signal-to-noise ratios are expected at the two edges.

The X-ray resonant-scattering intensity around the Gd $L_3$ edge was measured by scanning the grazing angle at the sample and keeping the detector fixed. The critical angle for total external reflection as well as the Kiessig fringes related to the film thickness can be clearly identified over the whole energy range (Fig. 6). This result matches very well the calculations based on the multilayer structure. The total

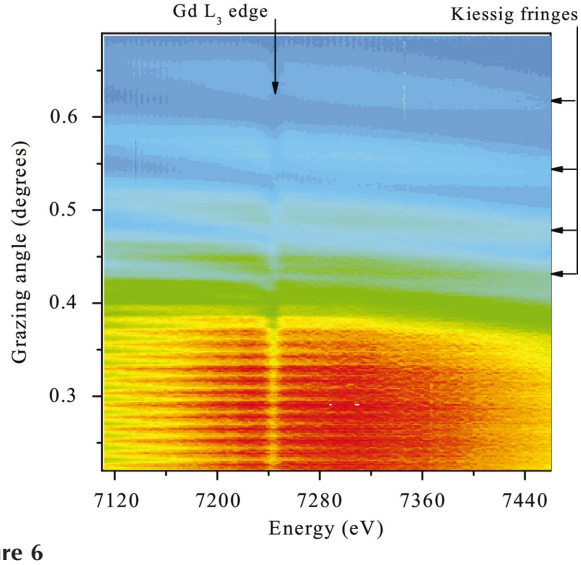


**Figure 6**
X-ray resonant scattering intensity around the Gd $L_3$ edge for the multilayer structure $(Co_{1\,nm}/Gd_{0.2\,nm})_{40}$ over $SiO_2$. The edge is indicated by the vertical arrow. Kiessig fringes are also indicated by lateral arrows.

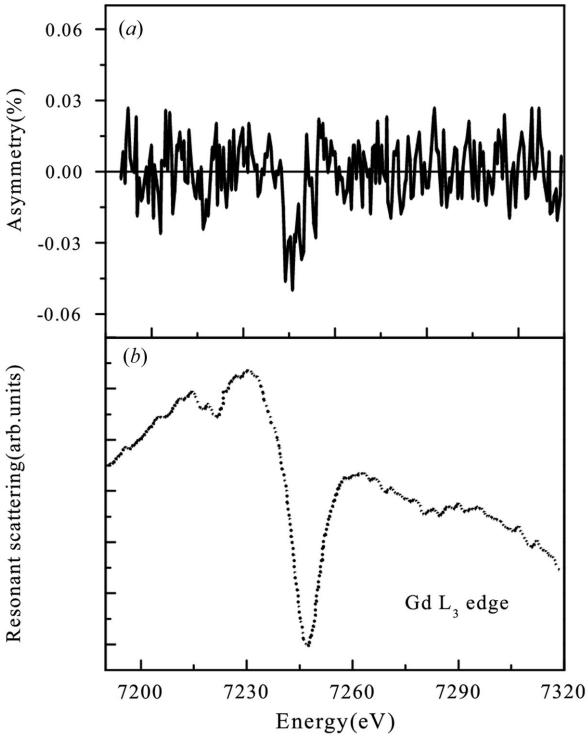


**Figure 7**
Intensity asymmetry ratio (*a*) and X-ray resonant scattering (*b*) at the Gd $L_3$ edge for the multilayer structure $(Co_{1\,nm}/Gd_{0.2\,nm})_{40}$ over $SiO_2$. The beam of about 80% circularly polarized photons reaches the sample with a grazing angle of 0.38°.

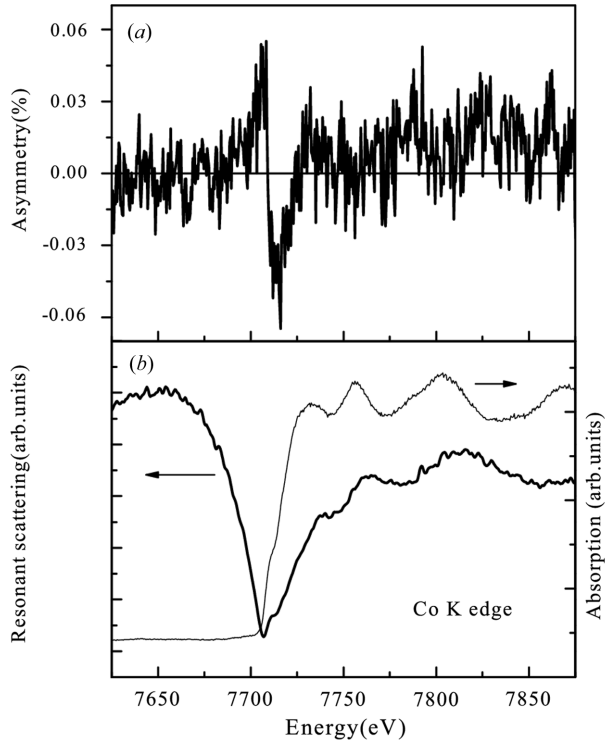


**Figure 8**
Intensity asymmetry ratio (*a*) and X-ray resonant scattering (*b*) at the Co *K* edge for the multilayer structure $(Co_{1\,nm}/Gd_{0.2\,nm})_{40}$ over $SiO_2$. The beam of about 70% circularly polarized photons reaches the sample with a grazing angle of 0.49°. The absorption cross section for Co metallic foil in transmission mode is also shown in (*b*).

collection time of the two-dimensional figure was around 15 min.

For the magnetic measurements at the Gd $L_3$ edge, the circularly polarized radiation was selected at 0.18 mrad ($\gamma\Psi \simeq 0.49$) above the orbit plane. The intensity, compared with the maximum at the orbit plane, was reduced by a factor of 3 and an elliptically polarized beam with about 80% of circular polarization rate was expected (Fig. 4). The grazing incidence angle was set close to the critical angle of reflection at $\alpha \simeq 0.38°$. The superior stability of the dispersive set-up enables the collection of dichroic spectra over a wide energy range with a noise smaller than 0.03%. An asymmetry ratio of about 0.05% is identified after a few minutes of acquisition (Fig. 7). The total collection time of this spectrum was less than 10 min, with four spectra of 100 s each.

At the Co *K* edge the circularly polarized radiation was selected at 0.14 mrad ($\gamma\Psi \simeq 0.38$) above the orbit plane. The intensity was reduced by a factor of 2 compared with the maximum at $\Psi = 0$ and an elliptically polarized beam with about 70% of circular polarization rate was expected. The grazing incidence angle was set close to the critical angle of reflection at $\alpha \simeq 0.49°$. The noise level was about 0.01% after collection of 128 spectra of 30 s each. An asymmetry ratio of about 0.5% is identified after 1 h of acquisition (Fig. 8).

We should emphasize that XRMS experiments using the dispersive XAS set-up combine two major advantages: the versatility of sample environment owing to the simple atmospheric working condition in the hard X-ray range, and absence of movements during acquisition characteristic of dispersive set-up.

## 6. Concluding remarks

We have given an overview of the prominent aspects of the polarization of the light delivered by a bending magnet, and some dichroic properties in X-ray absorption spectroscopy. We presented two applications using the two XAS beamlines at LNLS. The first example was a combination of experimental measurements and *ab initio* calculations of angle-resolved X-ray absorption, using linearly polarized light to investigate the local scale structural distortion induced by substrate strain in $La_{0.7}Sr_{0.3}MnO_6$ films. The analysis of the dichroic experimental data enables the derivation of a model of local distortion of the coordination shell around the Mn atoms, without any modification of the tilt angle Mn—O—Mn. In the second example we showed the feasibility of XRMS experiments in thin multilayers using the dispersive XAS set-up, to obtain information on local magnetic moments of rare-earths and transition metal oxides, using the circularly polarized light delivered by a bending magnet. These preliminary experiments open the way for more complex studies involving *in situ* conditions, like growth processes or thermal annealing, taking

advantage of the versatility of sample environment and the remarkable experimental stability.

We are very grateful to Maurizio Sacchi for providing the Gd/Co samples and for his invaluable support during the first XRMS experiments. We also acknowledge the LNLS technical staff, especially E. Tamura and R. Neueschwander, for their help in setting up the DXAS experiment, and F. C. Vicentin for his assistance in the calculations of light polarization. This work is partially supported by LNLS/ABTLuS/MCT and FAPESP (1999/12330-6). JCC, NMSN and AYR acknowledge the grants from FAPESP, CAPES and CNPq, respectively.

## References

Als-Nielsen, J. & McMorrow, D. (2001). *Refraction and Reflection from Interfaces*, ch. 3, pp. 61–106. New York: John Wiley and Sons.

Ankudinov, A. L., Bouldin, C., Rehr, J. J., Sims, J. & Hung, H. (2002). *Phys. Rev. B*, **65**, 104107.

Baudelet, F., Dartyge, E., Fontaine, A., Brouder, C., Krill, G., Kapller, J. P. & Piecuch, M. (1991). *Phys. Rev. B*, **43**, 5857–5866.

Brouder, C. (1990). *J. Phys. Condens. Matter*, **2**, 701–738.

Dartyge, E., Depautex, C., Dubuisson, J., Fontaine, A., Jucha, A., Leboucher, P. & Tourillon, G. (1986). *Nucl. Instrum. Methods A*, **246**, 452–460.

Dartyge, E., Fontaine, A., Tourillon, G., Cortes, R. & Jucha, A. (1986). *Phys. Lett. A*, **113**, 384–388.

DeGroot, F. M. F. (1994). *J. Electron Spectrosc. Relat. Phenom.* **67**, 529–622.

Ebert, H. (1996). *Circular Magnetic X-ray Dichroism in Transition Metal Systems*, pp. 159–177. Berlin: Springer.

Fontaine, A. (1993). *Interaction of X-rays with Matter: X-ray Absorption Spectroscopy*, Vol. I, ch. XV, pp. 323–369. Les Editions de Physique, Springer Verlag.

Fontcuberta, J., Martinez, B., Seffar, A., Pinol, S., Garcia-Munoz, J. & Obradors, X. (1996). *Phys. Rev. Lett.* **76**, 1122–1125.

Gaudry, E., Kiratisin, A., Sainctavit, P., Brouder, C., Mauri, F., Ramos, A., Rogalev, A. & Goulon, J. (2003). *Phys. Rev. B*, **67**, 094108.

Gibbs, D., Harshman, D. R., Isaacs, E., McWhan, D. B., Mills, D. & Vettier, C. (1988). *Phys. Rev. Lett.* **61**, 1241–1244.

Giles, C., Malgrange, C., Goulon, J., DeBergevin, F., Vettier, C., Dartyge, E., Fontaine, A., Giogetti, C. & Pizzini, S. (1994). *J. Appl. Cryst.* **27**, 232–240.

Giorgetti, C., Pizzini, S., Dartyge, E., Fontaine, A., Baudelet, F., Brouder, C., Bauer, P., Krill, G., Miraglia, S., Fruchart, D. & Kapler, J. P. (1993). *Phys. Rev. B*, **48**, 12732–12742.

Hannon, J. P., Trammell, G. T., Blume, M. & Gibbs, D. (1988). *Phys. Rev. Lett.* **61**, 1245–1248.

Haskel, D. (1998). PhD thesis. University of Washington, USA.

Heald, S. M. & Stern, E. A. (1977). *Phys. Rev. B*, **46**, 5549–5559.

Jackson, J. D. (1975). *Classical Electrodynamics*, ch. 14. New York: John Wiley and Sons.

James, R. W. (1965). *The Optical Principles of the Diffraction of X-rays*. London: G. Bell.

Jaouen, N., Tonnerre, J. M., Raoux, D., Bontempi, E., Ortega, L., Muenzenberg, Felsch, W., Rogalev, A., Durr, H. A., Dudzik, E., der Laan, G. V., Maruyama, H. & Suzuki, M. (2002). *Phys. Rev. B*, **66**, 134420/1–14.

Kao, C. C., Hastings, J. B., Johnson, E. D., Siddons, D. P., Smith, G. C. & Prinz, G. A. (1990). *Phys. Rev. Lett.* **65**, 373–377.

Koningsberger, D. C. & Prins, R. (1988). Editors. *X-ray Absorption – Principles, Applications, Techniques of EXAFS, SEXAFS and XANES*. New York: Wiley-Intersciences.

Magnan, H., Chandesris, D., Villette, B., Heckmann, O. & Lecante, J. (1991). *Phys. Rev. Lett.* **67**, 259–263.

Millis, A. J. (1998). *Nature (London)*, **392**, 147–150.

Millis, A. J., Darling, T. & Migliori, A. (1998). *J. Appl. Phys.* **83**, 1588–1591.

Natoli, C. (1984). *Distance Dependence of Continuum and Bound State of Excitonic Resonance in X-ray Absorption Near-Edge Structure (XANES)*, ch. 4, pp. 38–42. Berlin: Springer-Verlag.

Natoli, C. R., Misemer, D. K., Doniach, S. & Kutzler, F. W. (1980). *Phys. Rev. A*, **22**, 1104.

Pizzini, S., Baudelet, F., Chandesris, D., Fontaine, A., Magnan, H., George, J. M., Petroff, F., Barthelemy, A., Fert, A., Loloee, R. & Schroeder, P. A. (1992). *Phys. Rev. B*, **46**, 1253–1256.

Prellier, W., Lecoeur, P. & Mercey, B. (2001). *J. Phys. Condens. Matter*, **13**, R915–R944.

Ramos, A. Y., Souza-Neto, N. M., Giacomelli, C., Tolentino, H. C. N., Ranno, L. & Favre-Nicolin, E. (2003). *AIP Conf. Proc.* **652**, 456–461.

Ranno, L., Llobet, A., Tiron, R. & Favre-Nicolin, E. (2002). *Appl. Surf. Sci.* **188**, 170–175.

Raoux, D. (1993). *Introduction to Synchrotron Radiation and to the Physics of Storage Rings*, Vol. I, ch. II, pp. 37–78. Les Editions de Physique, Springer Verlag.

Rehr, J. J. & Albers, R. C. (2000). *Rev. Mod. Phys.* **72**, 621–654.

Rodrigues, A. R. D., Craievich, A. F. & da Silva, C. E. T. G. (1998). *J. Synchrotron Rad.* **5**, 1157–1161.

Sacchi, M., Hague, C. F., Pasquali, L., Mironi, A., Mariot, J. M., Isberg, P., Gullikson, E. M. & Unberwood, J. H. (1998). *Phys. Rev. Lett.* **81**, 1521–1524.

Salamon, M. B. & Jaime, M. (2001). *Rev. Mod. Phys.* **73**, 583–628.

Schütz, G., Wagner, W., Wilhelm, W. & Kienle, P. (1987). *Phys. Rev. Lett.* **58**, 737–740.

Seve, L., Jaouen, N., Tonnerre, J. M., Raoux, D., Bartolome, F., Arend, M., Felsch, W., Rogalev, A., Goulon, J., Gautier, C. & Berar, J. F. (1999). *Phys. Rev. B*, **60**, 9662–9674.

Souza-Neto, N. M., Ramos, A. Y., Tolentino, H. C. N., Favre-Nicolin, E. & Ranno, L. (2003). *Appl. Phys. Lett.* **83**, 3587.

Souza-Neto, N. M., Ramos, A. Y., Tolentino, H. C. N., Favre-Nicolin, E. & Ranno, L. (2004*a*). *J. Alloy. Compd.* **369**, 205–208.

Souza-Neto, N. M., Ramos, A. Y., Tolentino, H. C. N., Favre-Nicolin, E. & Ranno, L. (2004*b*). *Phys. Scr.* In the press.

Souza-Neto, N. M., Ramos, A. Y., Tolentino, H. C. N., Favre-Nicolin, E. & Ranno, L. (2004*c*). *Phys. Rev. B*, **70**, 174451.

Stern, E. A. (1974). *Phys. Rev. B*, **10**, 3027–3037.

Tolentino, H., Baudelet, F., Fontaine, A., Gourieux, T., Krill, G., Henry, J. Y. & Rossat-Mignod, J. (1992). *Physica C*, **192**, 115–130.

Tolentino, H. C. N., Cezar, J. C., Souza-Neto, N. M., Tamura, E., Ramos, A. Y. & Neueschwander, R. (2004). In preparation.

Tolentino, H. C. N., Cezar, J. C., Watanabe, N., Piamonteze, C., Souza-Neto, N. M., Tamura, E., Ramos, A. Y. & Neueschwander, R. (2004). *Phys. Scr.* In the press.

Tolentino, H. C. N., Ramos, A. Y., Alves, M. C. M., Barrea, R. A., Tamura, E., Cezar, J. C. & Watanabe, N. (2001). *J. Synchrotron Rad.* **8**, 1040–1046.

Tonnerre, J. M., Seve, L., Raoux, D., Soullie, G., Rodmacq, B. & Wolfers, P. (1995). *Phys. Rev. Lett.* **75**, 740–743.